

Epitaxially Strained CeO₂/Mn₃O₄ Nanocrystals as an Enhanced Antioxidant for Radioprotection

Sang Ihn Han, Sang-woo Lee, Min Gee Cho, Ji Mun Yoo, Myoung Hwan Oh, Beomgyun Jeong, Dokyoon Kim, Ok Kyu Park, Junchul Kim, Eun Namkoong, Jinwoung Jo, Nohyun Lee, Chaehong Lim, Min Soh, Yung-Eun Sung, Jongman Yoo, Kyungpyo Park,* and Taeghwan Hyeon*

Nanomaterials with antioxidant properties are promising for treating reactive oxygen species (ROS)-related diseases. However, maintaining efficacy at low doses to minimize toxicity is a critical for clinical applications. Tuning the surface strain of metallic nanoparticles can enhance catalytic reactivity, which has rarely been demonstrated in metal oxide nanomaterials. Here, it is shown that inducing surface strains of CeO₂/Mn₃O₄ nanocrystals produces highly catalytic antioxidants that can protect tissue-resident stem cells from irradiation-induced ROS damage. Manganese ions deposited on the surface of cerium oxide (CeO₂) nanocrystals form strained layers of manganese oxide (Mn₃O₄) islands, increasing the number of oxygen vacancies. CeO₂/Mn₃O₄ nanocrystals show better catalytic activity than CeO₂ or Mn₃O₄ alone and can protect the regenerative capabilities of intestinal stem cells in an organoid model after a lethal dose of irradiation. A small amount of the nanocrystals prevents acute radiation syndrome and increases the survival rate of mice treated with a lethal dose of total body irradiation.

The increasing use of ionizing radiation in medicine and industry has raised the risk of accidental total body irradiation (TBI), which can result in life-threatening consequences, such as acute radiation syndrome (ARS).^[1] Depending on the radiation exposure dose, ARS is categorized into hematopoietic (H-ARS, 1.5–4 Gy),

gastrointestinal (GI-ARS, 6–15 Gy), and neurovascular syndromes (NV-ARS, 15 Gy), which all involve the rapid generation of reactive oxygen species (ROS) in the tissues within a millisecond via the radiolysis of water, causing both acute and chronic oxidative damages to the cells and organs.^[2] Although Amifostine (Ethyol) was developed as a radioprotectant,^[3] its application is only approved for the protection of salivary glands, because its short elimination half-life and limited ROS-scavenging capacity require a high dose, which may cause systemic toxicity and complications, to be used under TBI conditions.^[4] In light of this, long-lasting radioprotectants with improved ROS-scavenging activities are highly desired.


In recent years, catalytic nanomaterials with antioxidant properties, such as cerium oxide,^[5] manganese oxide,^[6] and vanadium oxide^[7] (collectively known as nanozymes)^[8] have gained increasing attention for their ability to treat ROS-related diseases.^[9] In particular, CeO₂ nanoparticles have been used as efficient antioxidants because their ability to cycle between Ce³⁺ and Ce⁴⁺ ionic states allows them to catalytically

Dr. S. I. Han, M. G. Cho, J. M. Yoo, Dr. M. H. Oh, Dr. O. K. Park, J. Jo, C. Lim, Dr. M. Soh, Prof. Y.-E. Sung, Prof. T. Hyeon
Center for Nanoparticle Research
Institute for Basic Science (IBS)
Seoul 08826, Republic of Korea
E-mail: thyeon@snu.ac.kr

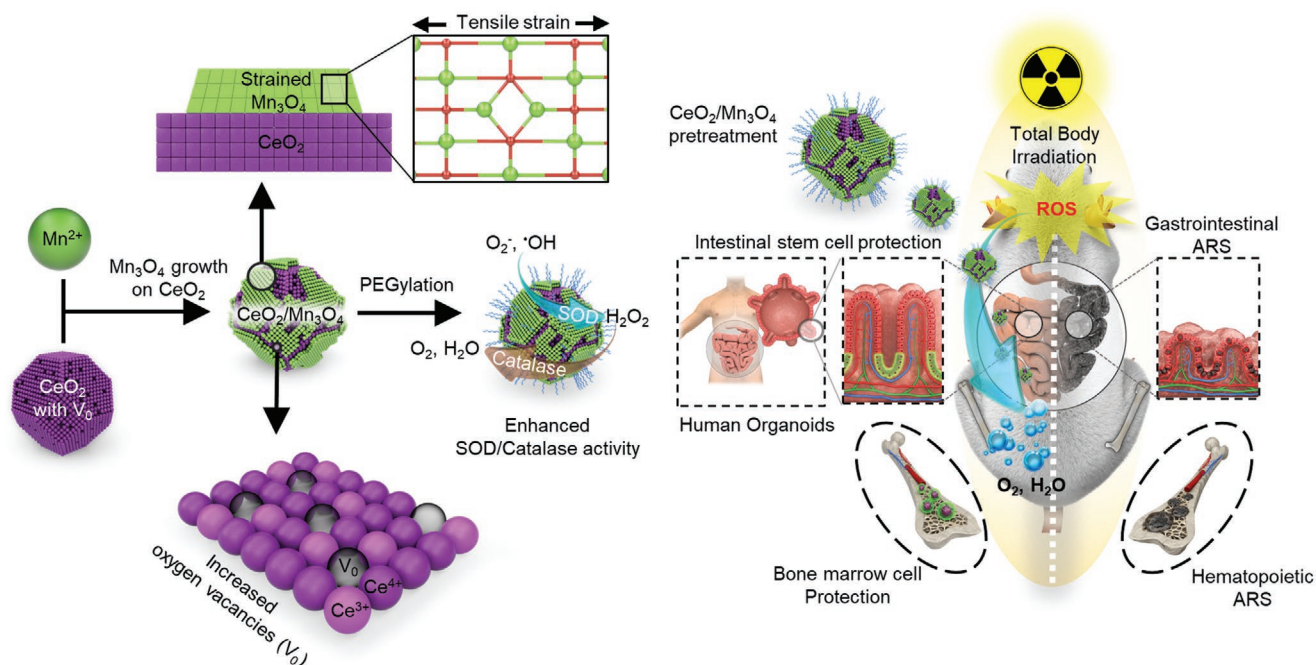
Dr. S. I. Han, M. G. Cho, J. M. Yoo, Dr. M. H. Oh, Dr. O. K. Park, J. Jo, C. Lim, Dr. M. Soh, Prof. Y.-E. Sung, Prof. T. Hyeon
School of Chemical and Biological Engineering
Institute of Chemical Processes
Seoul National University
Seoul 08826, Republic of Korea

S.-w. Lee, J. Kim, E. Namkoong, Prof. K. Park
Department of Physiology
School of Dentistry and Dental Research Institute
Seoul National University
Seoul 03080, Republic of Korea
E-mail: kppark@snu.ac.kr

Dr. B. Jeong
Advanced Nano Surface Research Group
Korea Basic Science Institute
Daejeon 34133, Republic of Korea
Prof. D. Kim
Department of Bionano Engineering and Bionanotechnology
Hanyang University
Ansan 15588, Republic of Korea
Prof. N. Lee
School of Advanced Materials Engineering
Kookmin University
Seoul 136-702, Republic of Korea
Prof. J. Yoo
Department of Microbiology
School of Medicine
CHA University
Sungnam 13488, Republic of Korea

 The ORCID identification number(s) for the author(s) of this article can be found under <https://doi.org/10.1002/adma.202001566>.

DOI: 10.1002/adma.202001566



Scheme 1. Schematic illustration of highly catalytic CeO₂/Mn₃O₄ nanocrystals preventing acute radiation syndrome.

remove various ROS, such as superoxide (O₂⁻), hydrogen peroxide (H₂O₂), and hydroxyl radical (·OH).^[10] However, the potential side effects of inorganic nanomaterials remain a critical issue,^[11] leading to the necessity of decreasing their administration while maintaining the therapeutic efficacy. One possible way is enhancing the catalytic reactivity of nanomaterials through ligand and strain effects.^[12] Notably, tuning the oxygen binding energy by modifying the surface strains of metallic core–shell nanomaterials has been shown to effectively enhance their catalytic activities.^[13] Such strain effects have rarely been demonstrated for inorganic nanozymes that scavenge ROS. We hypothesize that it is possible to lower the required doses of nanozyme-based therapeutic agents by imposing surface strains and improving their catalytic performance.

Here, we provide the proof of concept of the hypothesis by using CeO₂/Mn₃O₄ nanocrystals as a model system (**Scheme 1**). Manganese ions deposited on the surface of CeO₂ nanocrystals form islands of strained Mn₃O₄ layers and increase the numbers of oxygen vacancies in the CeO₂ phase. We demonstrate that these effects facilitate the redox reactions at the Mn₃O₄ and CeO₂ surfaces, enhancing the catalytic antioxidant activities. A mouse model study also revealed that a systemic delivery of a low dose of the nanocrystals can effectively protect the tissues from TBI.

Heterostructured CeO₂/Mn₃O₄ nanocrystals were prepared by a seed-mediated growth process.^[14] The seeds, 4 nm sized truncated octahedral CeO₂ nanocrystals, predominantly enclosed by {100} and {111} (**Figure 1a**), were reacted with MnCl₂ to yield the

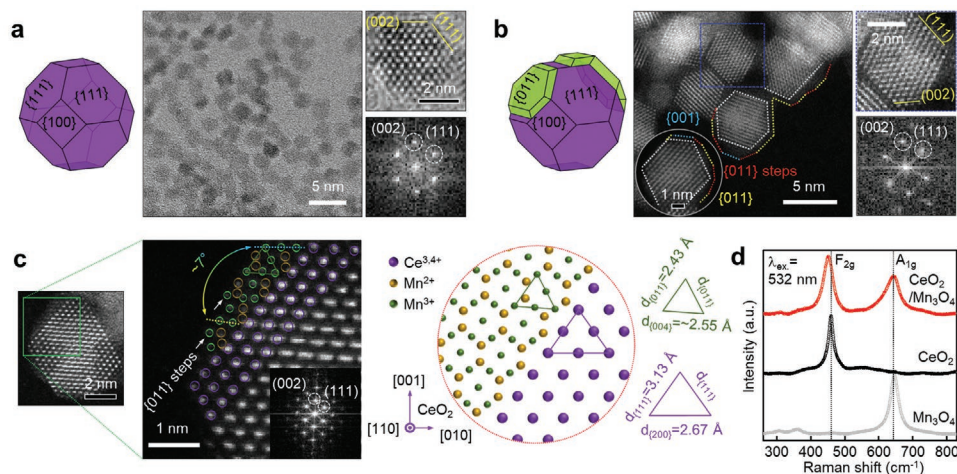


Figure 1. Morphology and atomic arrangement of heterostructured CeO₂/Mn₃O₄ nanocrystals. a,b) 3D illustration (left), TEM and STEM images (middle and top right), and the corresponding FFT pattern (bottom right) of CeO₂ nanocrystals (a) and CeO₂/Mn₃O₄ nanocrystals (b). c,d) Atomic-resolution STEM images (c) and visible Raman spectra (d) of CeO₂/Mn₃O₄ nanocrystals.

CeO₂/Mn₃O₄ nanocrystals (Figure 1b; and Figure S1, Supporting Information). High-angle annular dark-field scanning transmission electron microscopy (HAADF-STEM) images and the corresponding fast Fourier transform (FFT) image show that the core is well preserved after the heterogeneous precipitation of manganese oxide on the surface (Figure 1b). X-ray diffraction analysis reveals that the CeO₂ nanocrystals have the cubic fluorite structure (JCPDS #34-0394) with an estimated (111) spacing of 3.14 Å (Figure S2, Supporting Information). Crystallographic orientation between the CeO₂ core and Mn₃O₄ islands is illustrated in Figure 1c based on the *d*-spacings measured from the HAADF-STEM images. Given the lattice parameters of bulk CeO₂ {200} and Mn₃O₄ {004} (2.71 and 2.36 Å, respectively), the estimated lattice mismatch is ≈13%. Because of this large mismatch, Mn₃O₄ islands experience a tensile strain to have expanded Mn₃O₄ {004} lattice (≈2.55 Å). As the islands grow vertically, the highly strained Mn₃O₄ lattice gradually relaxes near the surface, as exemplified by those two nonparallel Mn₃O₄ {004} with the lattice angle difference of ≈7° (Figure 1c). This is further supported by the visible Raman characterization, which shows the peaks for the first-order F_{2g} symmetry mode of CeO₂ at 452 cm⁻¹ and the A_{1g} symmetric stretching of Mn–O bond in Mn₃O₄ at 645 cm⁻¹ (Figure 1d). Asymmetric broadening of the F_{2g} and A_{1g} peaks indicate the presence of defects and structural distortions induced by the heteroepitaxial strain.

When less than 15 mol% of Mn is deposited onto the CeO₂ nanocrystals, the oxidation state of Mn is mostly Mn²⁺ (“Mn thin” in Figure 2a; and Figure S3, Supporting Information). The reason Mn²⁺ motif deposits before the Mn³⁺ motif is because

the ionic radius of Mn²⁺ is more compatible with Ce⁴⁺.^[15] However, as more Mn is deposited, both Mn²⁺ and Mn³⁺ are observed (“CeO₂/Mn₃O₄” in Figure 2a). The lower intensity ratio of the Mn L₃- to L₂-edge (*I*(L₃/L₂)) absorption indicates the higher oxidation state of the Mn ions in CeO₂/Mn₃O₄. Interestingly, the Mn²⁺ peak is less pronounced than that of the previously reported bulk Mn₃O₄,^[16] showing that the strained Mn₃O₄ layers have slightly higher oxidation state than monometallic Mn₃O₄ nanocrystals. X-ray photoelectron spectroscopy (XPS) and X-ray absorption spectra (XAS) analyses jointly reveal that the Ce⁴⁺ ions in the CeO₂ nanocrystals and the deposited Mn²⁺ ions form a polar Ce⁴⁺–O–Mn²⁺ interface (Figure 2b; and Figure S4, Supporting Information). These data suggest that CeO₂/Mn₃O₄ nanocrystals are composed of CeO₂ core, Ce⁴⁺–O–Mn²⁺ heterointerface, and highly strained Mn₃O₄ islands.

The surface defect states of CeO₂ and CeO₂/Mn₃O₄ nanocrystals were compared using UV Raman spectroscopy (Figure 2c). The intensity ratio of the defect-induced (D mode) peak at 598 cm⁻¹ to F_{2g} peak at 452 cm⁻¹ (*I*_D/*I*_{F_{2g}}) increases after the Mn₃O₄ deposition, indicating that the number of oxygen vacancies increases on the surface of the CeO₂ nanocrystals. Such nanocrystals with abundant oxygen vacancies are expected to have improved ROS scavenging activities.^[17] O 1s XPS spectra further verifies the defective oxide surface (Figure 2d). The higher ratio of oxygen defects to lattice oxygen in CeO₂/Mn₃O₄ nanocrystals (0.85) compared to CeO₂ nanocrystals (0.60) results from the higher oxygen vacancy level, which agrees with the UV Raman results.

To evaluate the surface reducibility of the nanocrystals, we performed temperature-programmed reduction experiments

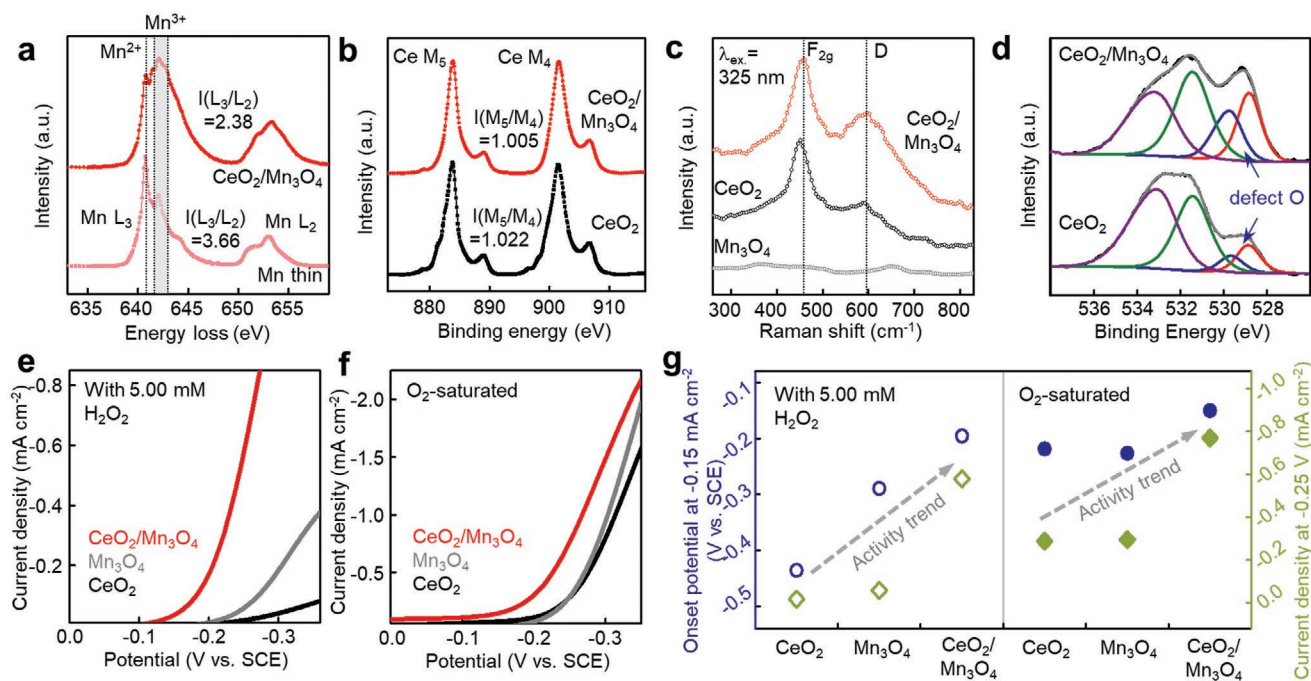


Figure 2. Structural characterization and electrocatalytic properties of heterostructured CeO₂/Mn₃O₄ nanocrystals. a) Mn L-edge XAS data of thin and optimized Mn oxide layer. b) Ce M-edge XAS analysis of CeO₂/Mn₃O₄ nanocrystals. c) UV Raman spectra of CeO₂/Mn₃O₄, CeO₂, and Mn₃O₄ nanocrystals. d) O 1s XPS spectra with binding energies assigned to lattice oxygen (≈529 eV, red), oxygen defects (≈530 eV, blue), surface adsorbed oxygen (≈531 eV, green), and surface oxygen (≈533 eV, purple). e, f) LSV curves for H₂O₂ reduction in Ar-saturated PBS (e) or oxygen reduction in O₂-saturated PBS (f). g) H₂O₂ and oxygen reduction activities in terms of onset potential and current density.

with H₂ (Figure S5, Supporting Information). Compared with the oxygen reduction peaks for CeO₂ (507 °C) and Mn₃O₄ (498 °C) nanocrystals, the peak for CeO₂/Mn₃O₄ nanocrystals is significantly shifted to a lower temperature (382 °C), indicating an enhanced surface reducibility (see Figure S6 in the Supporting Information for detailed Mn₃O₄ characterization). The abilities of each type of nanocrystal and the reference samples to eliminate ROS were further evaluated by measuring electrocatalytic reduction of H₂O₂ and oxygen. Linear-sweep voltammetry (LSV) was performed with the nanocrystals supported on glassy carbon electrode either in Ar-saturated phosphate-buffered saline (PBS, 0.01 M) containing 5×10^{-3} M H₂O₂ or in O₂-saturated PBS (Figure 2e,f). The measured catalytic activities were compared in terms of onset potential (measured at -0.15 mA cm⁻²) and current density (measured at -0.25 V) (Figure 2g). The larger onset potential and current density values observed for CeO₂/Mn₃O₄ nanocrystals clearly demonstrate their higher catalytic reduction activities than those of CeO₂ or Mn₃O₄ nanocrystals. Moreover, the CeO₂/Mn₃O₄ nanocrystals with the Mn₃O₄ islands exhibit a higher activity than those with thinner Mn₃O₄ layer or with Mn₃O₄ shell that covers most of the CeO₂ surface (Figure S7, Supporting Information). This indicates that the enhanced activity originates from the synergistic effect by the exposed CeO₂ surface and the highly strained Mn₃O₄ islands. Further, superoxide dismutase (SOD)- and catalase-mimetic assays showed similar ROS-scavenging trends to electrocatalytic tests (Figure S8a,b, Supporting Information). However, the ROS-scavenging activity of CeO₂/Mn₃O₄ nanocrystals decreased at lower pH (Figure S8c; and Section S1.1, Supporting Information). The as-synthesized hydrophobic CeO₂/Mn₃O₄ nanocrystals were transferred to PBS using the PEGylation method^[18] (Figure S9a, Supporting Information), and the PEGylated nanocrystals showed an average hydrodynamic diameter of ≈ 10 nm (Figure S9b, Supporting Information). The synthesized CeO₂/Mn₃O₄ nanocrystals in aqueous solution showed no significant cellular toxicity up to 176×10^{-6} M (Figure S9c, Supporting Information).

Among the three types of ARS, GI-ARS is generally manifests at radiation doses exceeding 6 Gy in humans, resulting in patients often dying within 3 weeks.^[2] Consequences of GI-ARS include the destruction of the villi and the intestinal stem cell (ISC)-containing crypts, which are associated with the loss of cell regeneration capacity and the disruption of intestinal epithelial barrier.^[19] However, if a certain amount of leucine-rich repeat-containing G-protein coupled receptor 5-positive (LGR5+) ISCs survive after irradiation, damaged intestinal structures can be regenerated.^[20] Therefore, LGR5+ ISCs can be considered as the most critical cell population for the recovery after the radiation-induced intestinal damage. We used mouse and human intestinal organoid (mIO and hIO, respectively) models that resemble the in vivo intestinal anatomy and physiology^[21] to test how well the CeO₂/Mn₃O₄ nanocrystals protect the LGR5+ ISCs from lethal doses of ionizing radiation. The irradiated subjects pretreated with CeO₂/Mn₃O₄ nanocrystals (IRR+CeO₂/Mn₃O₄ group) were compared with the irradiated subjects that were not pretreated with the nanocrystals (IRR group) and irradiated subjects that were pretreated with either CeO₂ (IRR+CeO₂ group) or Mn₃O₄ (IRR+Mn₃O₄ group) nanocrystals. Control (CTRL) subjects were neither irradiated nor pretreated with any nanocrystals.

mIOs established from LGR5-GFP transgenic mice were cultured with various nanocrystals and irradiated with a lethal dose (8 Gy). The morphology of the mIOs, the expression of proliferation marker (Ki67), the LGR5+ ISC population, were examined. Significantly more crypt buds and Ki67+ proliferative cells could be seen in the IRR+CeO₂/Mn₃O₄ group than the IRR+CeO₂ or IRR+Mn₃O₄ groups (Figure 3a; and Figure S10, Supporting Information). Although the bud morphology and number were partially preserved in the IRR+CeO₂ and IRR+Mn₃O₄ groups, very few Ki67+ cells were found, indicating a lower regenerative capacity. On the other hand, crypt buds and Ki67+ cells were completely eradicated in the IRR group. Fluorescence-activated cell sorting (FACS) analysis of LGR5+ ISCs also shows similar tendency. Approximately 14% of mIOs were LGR5+ in the CTRL group, but these cells were completely destroyed in the IRR group (0.17%) (Figure 3b; and Figure S11, Supporting Information). LGR5+ ISCs in the IRR+CeO₂/Mn₃O₄ group showed a significantly improved survival rate (9.78%) than those for the IRR+CeO₂ (4.82%) and IRR+Mn₃O₄ (2.54%) groups.

We further examined the radioprotective mechanism of CeO₂/Mn₃O₄ nanocrystals using hIO models. Because the radiation damage on cells and organs typically starts with an abnormal spike in ROS generation by the radiolysis of water, we tested whether CeO₂/Mn₃O₄ nanocrystals can effectively scavenge the radiation-induced intracellular ROS. Six hours after exposure to a lethal dose of irradiation (10 Gy), the ROS levels in hIOs increased in the IRR group, but such increase was suppressed in the IRR+CeO₂/Mn₃O₄ group (Figure S12, Supporting Information). At 24 h postirradiation, the IRR group showed a significant apoptotic activity as marked by the increased expression of cleaved caspase 3/7, while the IRR+CeO₂/Mn₃O₄ group showed dramatically reduced apoptotic areas that were limited to only a few peripheral crypts (Figure S13, Supporting Information).

To observe the effects of CeO₂/Mn₃O₄ nanocrystals on the acute molecular events occurring between the radiation-induced ROS elevation and the apoptosis, we performed mRNA sequencing at 12 h postirradiation. The global expression patterns of genes with statistical significance were visually presented by volcano plots (Figure 3c), a heat map with a hierarchical clustering dendrogram (Figure S14, Supporting Information), and a Venn diagram (Figure S15, Supporting Information). The IRR group showed greater changes in the gene expression than the IRR+CeO₂/Mn₃O₄ group with respect to the CTRL group. To further identify the genes that may affect the phenotypes seen in the organoids, we filtered out the genes that have expression volumes ≥ 4 . Totals of 31 up-regulated and 29 down-regulated genes in the IRR group were identified and the expressional fold change (FC) values of those genes in IRR or IRR+CeO₂/Mn₃O₄ versus CTRL were visualized via a heatmap (Figure 3d). To determine which biological functions these genes affected, we conducted a Gene Ontology analysis using false discovery rate (Figure S16, Supporting Information). The genes up-regulated by the irradiation were found to be mostly related to the cellular stress and the p53-mediated apoptotic process, while the down-regulated ones are mostly related to mitosis and the positive regulation of wingless/integrated (Wnt) signaling, which is known to be crucial for maintaining

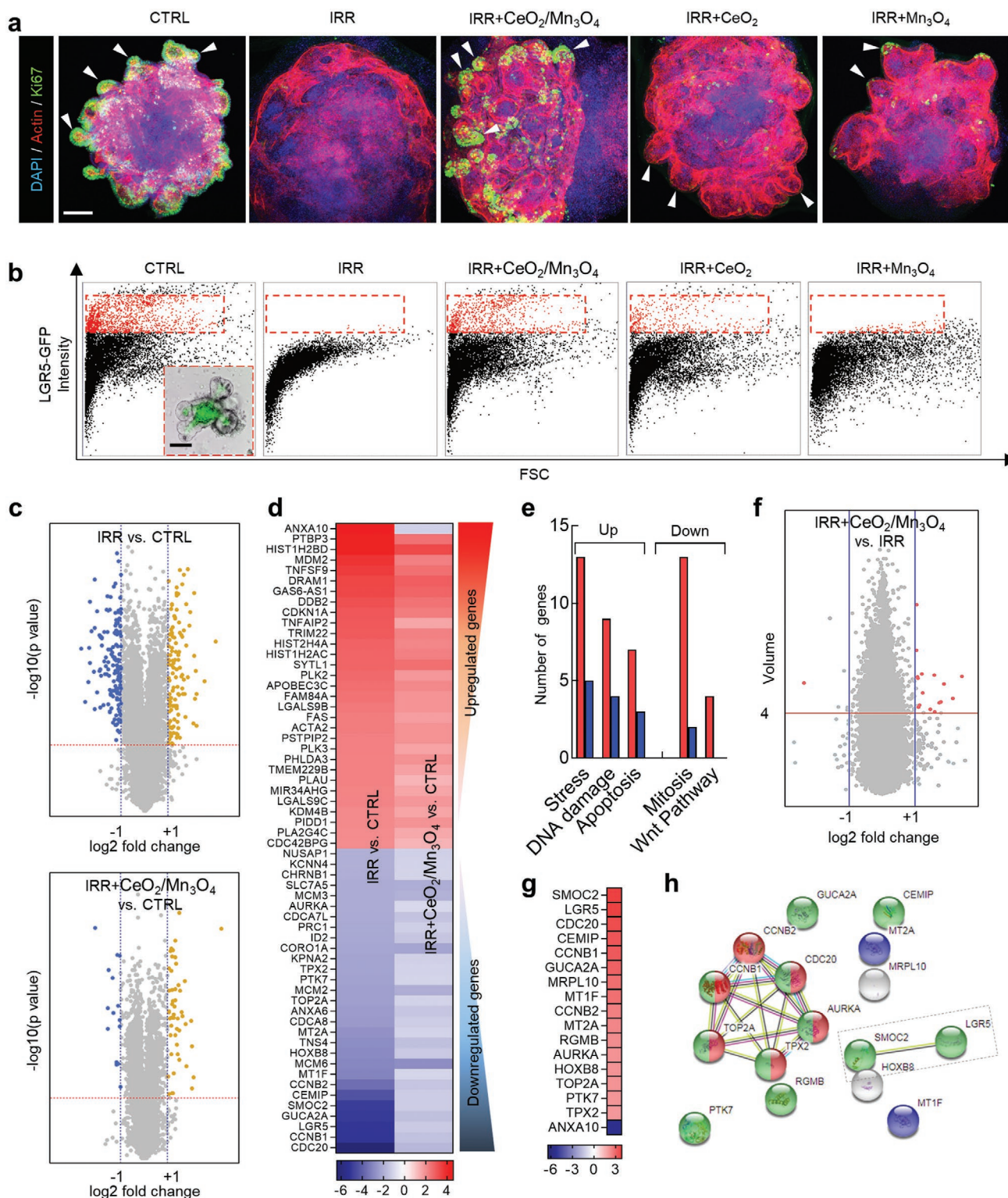


Figure 3. Radioprotective effects of CeO₂/Mn₃O₄ nanocrystals on intestinal stem cells in mouse and human organoid model. a) Confocal images of cells stained with Ki67, DAPI, and actin. Scale bar = 200 μ m. The white arrow heads indicate representative crypt buds. b) FACS analysis of dissociated LGR5-GFP miOs 48 h after irradiation (scale bar = 50 μ m). c) Volcano plot comparing the gene expression of IRR versus CTRL (top) and IRR+CeO₂/Mn₃O₄ versus CTRL (bottom). d) Genes showing more than twofold changes ($|FC| \geq 2$) with expression volume ≥ 4 in IRR versus CTRL (left column) and IRR+CeO₂/Mn₃O₄ versus CTRL (right column). e) The number of genes that were upregulated (left) and down-regulated (right) in IRR versus CTRL and IRR+CeO₂/Mn₃O₄ versus CTRL. f) Scatter plot comparing the gene expression patterns of IRR and IRR+CeO₂/Mn₃O₄ groups. g) Red colored genes in (f) are listed and ordered in a heat map based on their expression levels. h) Pathway analysis and categorization of the genes listed in (g) based on GO terms.

LGR5+ ISCs.^[22] Based on these gene ontologies, the number of genes that were significantly altered was compared between IRR and IRR+CeO₂/Mn₃O₄ versus CTRL. The pretreatment with CeO₂/Mn₃O₄ nanocrystals resulted in fewer numbers of stress-, DNA damage-, and p53 signal-related genes being up-regulated (4 vs 13, 3 vs 7, and 2 vs 6, respectively) (Figure 3e). More importantly, fewer numbers of the genes that are related to mitosis and the canonical Wnt pathway were down-regulated.

To further confirm the radioprotective effects of the CeO₂/Mn₃O₄ nanocrystal pretreatment, we compared the gene expression patterns of the IRR+CeO₂/Mn₃O₄ and IRR groups. 16 up-regulated and one down-regulated genes qualified the two criteria (FC ≥ 2 and expression volume ≥ 4, Figure 3f,g). Pathway analysis reveals that most of the genes up-regulated after the CeO₂/Mn₃O₄ nanocrystal pretreatment are related to the positive regulation of cellular processes (green beads in Figure 3h). Among them, CCNB1, CCNB2, CDC20, TOP2A, AURKA, and TPX2 are related to cell division (red or half-red beads in Figure 3h). SMOC2 and LGR5 are the positive regulators of the canonical Wnt pathway, and thus generally regarded as ISC signature genes (green dotted box in Figure 3h), while MT2A and MT1F genes are grouped as zinc-responsive antioxidant enzymes (blue beads in Figure 3h). These results suggest that although the pretreatment of CeO₂/Mn₃O₄ nanocrystals cannot fully prevent the irradiation-induced apoptosis for all the cell types, they can still reduce the damages to the LGR5+ ISC population, enabling them to regenerate in the damaged areas.

In prior to assess radioprotective efficacy *in vivo*, biocompatibility of CeO₂/Mn₃O₄ nanocrystal was examined in mice. The mice showed no abnormal histological alterations in the intestine, kidney, spleen, liver, heart, lung, and bladder (Figure S17a, Supporting Information) and no loss in body weight for up to 30 days after receiving a high dose (50 mg kg⁻¹) of CeO₂/Mn₃O₄ nanocrystals (Figure S17b, Supporting Information). These results demonstrate that the nanocrystals do not have any notable systemic toxicity.

To test the systemic radio-protective effects of the CeO₂/Mn₃O₄ nanocrystals, we intraperitoneally injected the mice with 0.55 mg nanocrystals kg⁻¹. Within an hour, the nanocrystals were successfully localized in the intestine and hematopoietic organs including the spleen and bone marrow (Figure S18, Supporting Information). The mice were then subjected to TBI (13 Gy) 1 h after the injection of the nanocrystals, and assays for evaluating H-ARS and GI-ARS were performed at the indicated time points (Figure 4a). Survival rate of the mice in IRR group decreased drastically after irradiation and all mice were dead at 13 days post-TBI. Surprisingly enough, when 400 mg kg⁻¹ of Amifostine was injected, which is effective dose for TBI but known to cause systemic toxicity, six out of ten mice died instantaneously, due to its toxicity (yellow highlight in Figure 4b).^[4] Among the remaining four mice, two mice survived 30 days after the TBI (Figure 4b). When the dose was reduced to 250 mg kg⁻¹, 20% survived 30 days after the TBI (Figure 4b). The monometallic CeO₂ nanocrystals and Mn₃O₄ nanocrystals showed a survival rates of 30% and 20%, respectively, indicating that they did not sufficiently protect the animals against 13 Gy TBI. However, animals in the IRR+CeO₂/Mn₃O₄ group showed survival rate of 67% up to 150 days after TBI (Figure 4b; and Figure S19, Supporting Information). The increased survival rate of the IRR+ CeO₂/Mn₃O₄ group can be

attributed to the ability of the nanocrystals to prevent systemic ROS damage that causes H-ARS and GI-ARS.

We estimated the ROS damage by measuring malondialdehyde (MDA), which is a toxic substance produced by lipid peroxidation,^[23] in plasma and five critical organs (small intestine, liver, kidney, spleen, and lung). The IRR+ CeO₂/Mn₃O₄ group showed ≈55% lower plasma MDA level than the IRR group 1 day after TBI (Figure 4c). Four days after TBI, the MDA levels in the five critical organs showed significant increases in the IRR group, whereas all the organs except the kidney did not show any statistically significant MDA level increase in the IRR+CeO₂/Mn₃O₄ group compared to the CTRL group (Figure 4d).

To assess the hematopoietic damages causing H-ARS, we measured the ROS levels in bone marrow cells (BMCs) of the different groups 30 min after TBI. Compared to the CTRL group, the IRR group showed a threefold increase in ROS level, whereas the IRR+CeO₂/Mn₃O₄ group showed only a 1.8-fold increase (Figure 4e,f). Three days after TBI, we isolated and counted the total BMCs. Nearly 95% of the BMCs in the femur were ablated in the IRR group, whereas only 52% were ablated in the IRR+CeO₂/Mn₃O₄ group (Figure 4g). Prevention of radiation-induced bone marrow ablation by CeO₂/Mn₃O₄ nanocrystals was further confirmed by haematoxylin & eosin (H&E) staining. Figure 4h depicts that the hematopoietic cellularity of IRR+ CeO₂/Mn₃O₄ group was significantly less damaged compared with that of IRR group. However, both monometallic nanocrystals of CeO₂ and Mn₃O₄, which have significantly lower cellularity than the IRR+CeO₂/Mn₃O₄ group, were unable to effectively protect the BMCs from irradiation (see Section S1.2 and Figure S20 in the Supporting Information for detailed explanation).

When intestinal damages causing GI-ARS were examined, we found that villi in the IRR group were severely impaired 5 days after TBI, whereas those in the IRR+CeO₂/Mn₃O₄ group remained long and intact (Figure 4i; and Figure S21, Supporting Information). Ki67 staining and TUNEL assay further show that the IRR+CeO₂/Mn₃O₄ group has higher mitotic activities accompanied with lower cell death than the IRR group, indicating the CeO₂/Mn₃O₄ nanocrystals protect the ISCs in the intestinal crypts (Figure 4j; and Figure S22, Supporting Information). Furthermore, histology and Ki67/TUNEL staining results further revealed that heterostructured CeO₂/Mn₃O₄ nanocrystals have a significantly better GI radioprotective capacity than monometallic CeO₂ or Mn₃O₄ nanocrystals (see Section S1.2 and Figure S22 in the Supporting Information for detailed explanation of the data). To evaluate the regenerative capacity of crypt ISCs after the irradiation, we isolated the crypts from the mice 30 min after TBI and cultured them in an *in vitro* intestinal organoid culture condition. Seven days after the seeding, the intestinal organoids generated from the crypts of the IRR+CeO₂/Mn₃O₄ group displayed normal organoid phenotypic characteristics, but the crypts from the IRR group failed to form organoids (Figure 4k; and Figure S23a,b, Supporting Information).

Organs from the mice that were pretreated with the CeO₂/Mn₃O₄ nanocrystals, and that had survived 150 days after TBI, were harvested and assessed for long-term damage. The jejunum of the survivors showed no sign of tumorigenesis or pathogenesis (Figure S24a, Supporting Information). The survivors also had similar villus lengths, crypt numbers, and fibrosis compared to the CTRL group (Figure S24a–f, Supporting

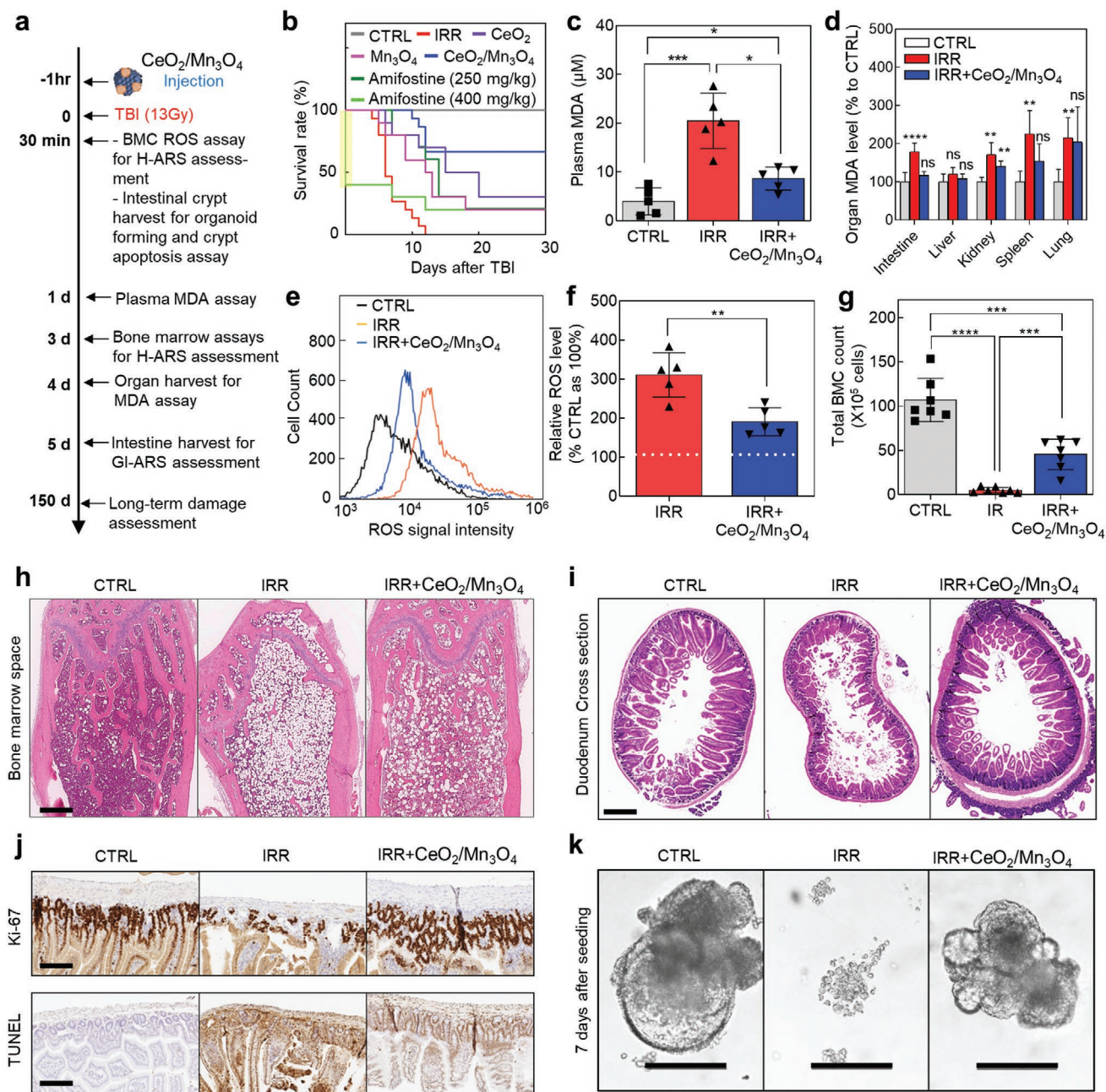


Figure 4. CeO₂/Mn₃O₄ nanocrystals prevent radiation-induced multiorgan damage in vivo. a) Timeline for in vivo radioprotection assays. b) Kaplan–Meier survival rates over 30 days after 13 Gy TBI ($n = 15$ for CTRL, IRR, and CeO₂/Mn₃O₄ group $n = 10$ for Amifostine, CeO₂, and Mn₃O₄ group). The yellow highlight indicates the immediate death of six mice due to toxicity of Amifostine. c) Plasma MDA concentration 1 day after TBI. d) Relative MDA levels of five critical organs 4 days after TBI ($n = 4–5$). e) FACS measurements of intracellular ROS levels of femoral BMCs at 30 min after TBI ($n = 5$). f) The FACS results from (e) are quantified and presented relative to the CTRL group ($n = 5$). g) Total number of remaining BMCs in the mouse femurs 3 days after TBI. h) H&E-stained femur sections 3 days after irradiation (scale bar = 500 μm). i) H&E staining of longitudinally sectioned duodena 5 days after irradiation (scale bar = 500 μm). j) Immunostaining of Ki67 cells (top row) and TUNEL assay for apoptotic or necrotic intestinal cells (bottom row) 5 days after TBI (scale bar = 200 μm). k) Bright field images of intestinal organoids formed by the crypts isolated 30 min after TBI and cultured for 7 days ($n = 3$, scale bar = 500 μm). Data were analyzed using unpaired *t*-test. Error bars denote mean ± standard error. Statistical significance is set as * $P < 0.05$, ** $P < 0.01$, *** $P < 0.001$, **** $P < 0.0001$; ns, not statistically significant.

Information). No sign of lung fibrosis was seen and the histology of the liver, spleen, and kidney was comparable to the CTRL group (Figure S25a–d, Supporting Information).

In summary, our results show that the antioxidant activity of heterostructured CeO₂/Mn₃O₄ nanocrystals is powerful enough

to protect the hematopoietic intestinal stem cells from irradiation-induced ROS damage. Manganese ions deposited on the surface of CeO₂ nanocrystals form the islands of epitaxially strained Mn₃O₄ layers, generating abundant oxygen vacancies in the CeO₂ phase. The increased number of oxygen vacancies

effectively improved the oxygen adsorption efficiency on the nanocrystal surface, allowing the nanocrystals to scavenge ROS more efficiently. We show that only a small dose of the CeO₂/Mn₃O₄ nanocrystals is required to protect the ICSs from the irradiation-induced ROS damage using a hIO model and mRNA sequencing. In the mouse model, a small dose of the CeO₂/Mn₃O₄ nanocrystals can effectively improve the survival rate after TBI. Our results demonstrate that the surface strain tuning of CeO₂ nanocrystals can enhance their antioxidant properties, making them highly effective radioprotectants for preventing ARS induced by TBI.

Experimental Section

A detailed description of procedures and characterization methods are available in the Supporting Information.

Supporting Information

Supporting Information is available from the Wiley Online Library or from the author.

Acknowledgements

S.I.H., S.-w.L., and M.G.C. contributed equally to this work. This work was supported by Institute for Basic Science (IBS-R006-D1) and National Research Foundation of Korea Grant No. (NRF-2018R1A2B3005113) at Seoul National University. Human intestinal organoids (hIOs) and Lgr5-GFP transgenic mouse intestinal organoids (mIOs) were obtained from Institute of Basic Medical Sciences, School of Medicine, CHA University, Seongnam, South Korea. hIOs or mIOs embedded in Matrigel were either cultured with Mouse Small Intestine Organoid Media (Organoid Science, Seoul, Korea) or Human Small Intestinal Organoid Media (Organoid Science, Seoul, Korea). For hIOs, the protocol was conducted in accordance with the Declaration of Helsinki and was approved by the institutional review board at CHA Bundang Hospital (IRB no. CHA-2018-05-024-011). All animal experiment protocols were approved by Seoul National University Institutional Animal Care and Use Committee (approval number: SNU-160322-2-3).

Conflict of Interest

The authors declare no conflict of interest.

Keywords

acute radiation syndrome, heterostructured nanocrystals, lattice strain, radioprotectants, reactive oxygen species

Received: March 5, 2020

Revised: May 8, 2020

Published online:

- [1] J. Xie, C. Wang, F. Zhao, Z. Gu, Y. Zhao, *Adv. Healthcare Mater.* **2018**, *7*, 1800421.
- [2] K. R. Brown, E. Rzuclidlo, *J. Vascul. Surg.* **2011**, *53*, 15S.
- [3] J. R. Kouvaris, V. E. Kouloulis, L. J. Vlahos, *Oncologist* **2007**, *12*, 738.
- [4] V. K. Singh, T. M. Seed, *Expert Opin. Drug Saf.* **2019**, *18*, 1077.
- [5] a) Q. Bao, P. Hu, Y. Xu, T. Cheng, C. Wei, L. Pan, J. Shi, *ACS Nano* **2018**, *12*, 6794; b) K. Korschelt, M. N. Tahir, W. Tremel, *Chem. – Eur. J.* **2018**, *24*, 9703; c) D. Jiang, D. Ni, Z. T. Rosenkrans, P. Huang, X. Yan, W. Cai, *Chem. Soc. Rev.* **2019**, *48*, 3683.
- [6] a) N. Singh, M. A. Savanur, S. Srivastava, P. D'Silva, G. Mughesh, *Angew. Chem., Int. Ed.* **2017**, *56*, 14267; b) B. Yang, Y. Chen, J. Shi, *Adv. Mater.* **2019**, *31*, 1901778.
- [7] F. Natalio, R. André, A. F. Hartog, B. Stoll, K. P. Jochum, R. Wever, W. Tremel, *Nat. Nanotechnol.* **2012**, *7*, 530.
- [8] a) L. Gao, J. Zhuang, L. Nie, J. Zhang, Y. Zhang, N. Gu, T. Wang, J. Feng, D. Yang, S. Perrett, X. Yan, *Nat. Nanotechnol.* **2007**, *2*, 577; b) G. Y. Tonga, Y. Jeong, B. Duncan, T. Mizuhara, R. Mout, R. Das, S. T. Kim, Y.-C. Yeh, B. Yan, S. Hou, V. M. Rotello, *Nat. Chem.* **2015**, *7*, 597; c) A. Ghosh, S. Basak, B. H. Wunsch, R. Kumar, F. Stellacci, *Angew. Chem., Int. Ed.* **2011**, *50*, 7900; d) R. Das, R. F. Landis, G. Y. Tonga, R. Cao-Milán, D. C. Luther, V. M. Rotello, *ACS Nano* **2019**, *13*, 229; e) T. Kang, Y. G. Kim, D. Kim, T. Hyeon, *Coord. Chem. Rev.* **2020**, *403*, 213092.
- [9] a) M. Liang, X. Yan, *Acc. Chem. Res.* **2019**, *52*, 2190; b) N. Singh, G. Mughesh, *Angew. Chem., Int. Ed.* **2019**, *58*, 7797; c) J. Wu, X. Wang, Q. Wang, Z. Lou, S. Li, Y. Zhu, L. Qin, H. Wei, *Chem. Soc. Rev.* **2019**, *48*, 1004.
- [10] a) M. Soh, D.-W. Kang, H.-G. Jeong, D. Kim, D. Y. Kim, W. Yang, C. Song, S. Baik, I.-Y. Choi, S.-K. Ki, H. J. Kwon, T. Kim, C. K. Kim, S.-H. Lee, T. Hyeon, *Angew. Chem., Int. Ed.* **2017**, *56*, 11399; b) B. Yang, Y. Chen, J. Shi, *Chem. Rev.* **2019**, *119*, 4881.
- [11] V. Cagno, P. Andreozzi, M. D'Alicarnasso, P. Jacob Silva, M. Mueller, M. Galloux, R. Le Goffic, S. T. Jones, M. Vallino, J. Hodek, J. Weber, S. Sen, E.-R. Janeček, A. Bekdemir, B. Sanavio, C. Martinelli, M. Donalisio, M.-A. Rameix Welti, J.-F. Eleouet, Y. Han, L. Kaiser, L. Vukovic, C. Tapparel, P. Král, S. Krol, D. Lembo, F. Stellacci, *Nat. Mater.* **2018**, *17*, 195.
- [12] a) M. Chen, D. Kumar, C.-W. Yi, D. W. Goodman, *Science* **2005**, *310*, 291; b) J. Zhang, M. B. Vukmirovic, Y. Xu, M. Mavrikakis, R. R. Adzic, *Angew. Chem., Int. Ed.* **2005**, *44*, 2132.
- [13] a) L. Bu, N. Zhang, S. Guo, X. Zhang, J. Li, J. Yao, T. Wu, G. Lu, J.-Y. Ma, D. Su, X. Huang, *Science* **2016**, *354*, 1410; b) M. Luo, S. Guo, *Nat. Rev. Mater.* **2017**, *2*, 17059.
- [14] a) M. H. Oh, T. Yu, S.-H. Yu, B. Lim, K.-T. Ko, M.-G. Willinger, D.-H. Seo, B. H. Kim, M. G. Cho, J.-H. Park, K. Kang, Y.-E. Sung, N. Pinna, T. Hyeon, *Science* **2013**, *340*, 964; b) M. H. Oh, M. G. Cho, D. Y. Chung, I. Park, Y. P. Kwon, C. Ophus, D. Kim, M. G. Kim, B. Jeong, X. W. Gu, J. Jo, J. M. Yoo, J. Hong, S. McMains, K. Kang, Y.-E. Sung, A. P. Alivisatos, T. Hyeon, *Nature* **2020**, *577*, 359.
- [15] C. Y. Kang, H. Kusaba, H. Yahiro, K. Sasaki, Y. Teraoka, *Solid State Ionics* **2006**, *177*, 1799.
- [16] M. Risch, K. A. Stoerzinger, B. Han, T. Z. Regier, D. Peak, S. Y. Sayed, C. Wei, Z. Xu, Y. Shao-Horn, *J. Phys. Chem. C* **2017**, *121*, 17682.
- [17] J.-D. Cafun, K. O. Kvashnina, E. Casals, V. F. Puentes, P. Glatzel, *ACS Nano* **2013**, *7*, 10726.
- [18] C. K. Kim, T. Kim, I.-Y. Choi, M. Soh, D. Kim, Y.-J. Kim, H. Jang, H.-S. Yang, J. Y. Kim, H.-K. Park, S. P. Park, S. Park, T. Yu, B.-W. Yoon, S.-H. Lee, T. Hyeon, *Angew. Chem., Int. Ed.* **2012**, *51*, 11039.
- [19] J. K. Waselenko, T. J. MacVittie, W. F. Blakely, N. Pesik, A. L. Wiley, W. E. Dickerson, H. Tsu, D. L. Confer, C. N. Coleman, T. Seed, P. Lowry, J. O. Armitage, N. Dainiak, *Ann. Intern. Med.* **2004**, *140*, 1037.
- [20] C. Metcalfe, N. M. Kljavin, R. Ybarra, F. J. de Sauvage, *Cell Stem Cell* **2014**, *14*, 149.
- [21] N. C. Zachos, O. Kovbasnjuk, J. Foulke-Abel, J. In, S. E. Blutt, H. R. de Jonge, M. K. Estes, M. Donowitz, *J. Biol. Chem.* **2016**, *291*, 3759.
- [22] N. Barker, J. H. van Es, J. Kuipers, P. Kujala, M. van den Born, M. Cozijnsen, A. Haegebarth, J. Korving, H. Begthel, P. J. Peters, H. Clevers, *Nature* **2007**, *449*, 1003.
- [23] F. Cruz-Guilloty, V. L. Perez, *Nature* **2011**, *478*, 42.